Hindawi
Geofluids
Volume 2023, Article ID 8870126, 22 pages
https://doi.org/10.1155/2023/8870126

Research Article

Progressive Evolution Model of Fault Water Inrush Caused by Underground Excavation Based on Multiphysical Fields

Xue Li, Yi Xue, and Zhihao Zhang

School of Civil Engineering and Architecture, Xi'an University of Technology, Xi'an 710048, China

Correspondence should be addressed to Yi Xue; xueyi@xaut.edu.cn

Received 4 February 2023; Revised 2 April 2023; Accepted 11 April 2023; Published 28 April 2023

Academic Editor: Tianshou Ma

Underground fault water inrushes are frequent hydrogeological disasters associated with underground mining and tunnel construction projects. In this study, we analyze the water inrush mechanism of underground engineering by building a numerical simulation model to evaluate the process of water inrush, analyze water inrush changes under various working conditions, and consider the fluid-solid coupling effect of rock mass and water. These analyses provide effective suggestions for preventing water inrush from faults. The study establishes a two-dimensional numerical model based on Darcy's law and plane strain field to analyze water inrush from faults in underground engineering. The analysis shows that factors such as aquifer pressure, permeability between the aquifer and fault zone, and permeability sensitivity coefficient are important considerations that affect the occurrence of water-inrush disasters. The study also identifies the sudden change in water inrush speed at the fault zone and the roadway when the working condition is changed as an indication of the nature of water inrush at the fault. Additionally, the study presents preventive measures such as drainage grouting to ensure the safety of underground engineering constructions. Overall, this research provides important insights into the causes and effects of water inrush from faults and can inform practical measures to mitigate the risks associated with underground engineering.

1. Introduction

Among the five major disasters causing coal mine production accidents, the degree of harm of a coal mine water disaster is only second to a gas explosion, and the economic loss caused by coal mine water inrush is the first [1, 2]. The problem of coal mine flooding has always been a major issue in coal mining and coal mine safety. However, due to the rapid growth of coal demand and demand worldwide, it is bound to generate more mining volumes, increasing the depth of mining. The geological and hydrogeological conditions of mining are becoming more complex, and the water inflow is increasing, causing serious flood problems [3, 4]. With the rapid development of China's mining industry, the complexity of fault disasters is increasing and it is also more difficult to detect, which makes fault water-inrush disasters more threatening. The fault will lead the aquifer to conduct water to the underground project construction area [5]. The fluid-solid coupling of the aquifer and rock in the underground project increases the difficulty of water-inrush disaster prevention. Disaster early warning is an important measure for disaster prevention and reduction [6]. Good monitoring can reduce casualties and economic losses caused by disasters and reduce the waste of social resources. At present, the decision-making of water-inrush prediction is not objective and accurate enough, and most of them are established based on the experience of the previous investigation [7]. On the one hand, during the survey, the actual situation may be fully investigated, and the experience and knowledge may not be comprehensive. On the other hand, water inrush changes from time to time, and the actual situation of the project is changeable, so it cannot be determined whether water inrush occurs by a single preliminary survey [8]. It is not accurate to make water inrush decisions for underground works only based on previous investigation and construction experience. It is important to monitor the water inrush in the early stage of coal mining [9] for preventing water inrush accidents, protecting the safe production of coal mines and improving the sustainable and rapid development of coal mine excavation. Therefore, this paper

analyzes and studies the possibility of water inrush from coal mine faults. The results of the numerical simulation can not only screen out the main factors affecting water inrush from coal seam faults and their degree of influence but also formulate a series of feasible mine water prevention measures based on them to effectively ensure safe production and improve the economic benefits of the mine when avoiding production accidents. Therefore, this paper establishes a fluid-solid coupling model, analyzes and simulates fault water inrush, and studies its main influencing factors. The conclusions can be used to prevent and monitor coal mine water inrush disasters to achieve safe production.

The research on mine water inrush in China began in the 1960s, initially taking coal mine floor water inrush as the research object [10]. The study of fault water inrush is no longer limited to basic theories such as hydrogeology and petrology but is verified by multidisciplinary and multimeans [11, 12]. Li et al. classified faults into open and closed ones according to their properties [13]. Generally speaking, the water inrush area of an open fault is caused by a large number of tension fractures between the hanging wall and footwall of the fault under the pressure of the aquifer, and the confined water flows into the roadway through the water diversion channel to produce water inrush. Closed faults induce instability in the strength between the key layers of the two walls of the fault under rock pressure [14, 15]. It is generally believed that the larger the fault size and the larger the drop, the greater the possibility of water inrush. However, it is not appropriate to measure the relative size of the probability of water inrush from a fault only by the size of the fault size and the drop, which are also related to other characteristics such as fault dip angle, the degree of fault rock cementation, and the strength of the two aquifers. Research shows that the normal fault with a low angle is more likely to induce water inrush because the damage degree of the former to surrounding rock is stronger than the latter. This method focuses on the basic theoretical study of faults and theoretically analyzes the water inrush process of faults by studying the characteristics of fault tectonite, occurrence, and other aspects. Hence, during the study of the fault characteristics essential for water inrush, an extensive amount of field-measured data, often influenced by various factors, is required [16, 17]. This necessitates a significant workload and a long measurement period. It is also unreasonable to infer other cases only from the water inrush process of a fault [18, 19]. The theory or formula obtained by this method also needs a lot of practice to verify.

The behavior of mining of coal seams in the stope and the fault fracture zone interact with each other. The mining stress represented by the abutment pressure is the main inducement for the formation of the water-conducting fracture zone due to the floor failure and the "activation" of the fault water inrush [20, 21]. At the same time, due to the influence of fracture, the stress distribution of surrounding rock in the stope and fracture area is more intensive, thus increasing the risk of floor instability [22]. The relevant simulation research shows that during the mining period, the water-conducting cracks caused by the basement fracture are mostly located in the rock mass at the end and lower part of the working face. In these two parts, the seepage rate is high, and they are the main channels for forming the outburst of water. Attention should be paid to the practical application [23–25]. The numerical simulation results of UDEC show that UDEC can not only reflect the geometric discontinuity characteristics of rock but also simulate the complex deformation of crack opening, sliding, caving, etc. At the same time, the stress permeability characteristics of rock are studied, and the compaction under the mine is predicted. The non-Darcy flow equation is applied in the fault fracture zone, and the influence of stress and pore water pressure on the rock mechanical parameters in the fault zone is considered [26, 27]. The results show that the Forchheimer equation of non-Darcy can effectively simulate and calculate the flow process of high-pressure and high-velocity water flow in the fault [28]. The fluid-solid coupling function has a significant impact on the non-Darcy flow characteristics in the fault. As the joint between the aquifer and the working face, the sudden change of the permeability of the fault fracture zone under the stress is the root cause of the formation of the fault water inrush. The fault is the main conduction area of the aquifer and working face [29, 30]. Under the stress condition, the change of its permeability is the main factor affecting the water inrush pressure and water inrush velocity. It is found that the permeability in the normal pressure zone decreases gradually as the stress in the fracture increases. At the boundary of the fault and the coal seam, there is an obvious stress relaxation zone, which increases the wellbore pressure drop and the seepage rate. When the mining reaches the edge of the fault, the stress is relieved. Permeability mutation in the formation is an important factor leading to fault activation [31].

The occurrence of water inrush accidents in coal mines is the result of multiple factors, and the law of accidents caused by these factors is discrete and nonlinear [32]. During the establishment of most models, many objective phenomena have been simplified which are inconsistent with reality, that is, the complex water inrush problem has been simplified [33]. The linear problem of a nonsingle variable is dealt with linearly and simply, so that the evaluation conclusion loses authority. At present, the prediction and prediction decision-making of water inrush in China are mostly based on the subjective evaluation of the geological data of the mine, which is difficult to ensure objectivity and comprehensiveness [34, 35]. At present, the safety assessment of domestic coal enterprises is mainly based on written documents, which are too theoretical to provide an effective decision-making basis for enterprise decision-makers. At present, the existing decision-making technologies for water inrush have their own advantages, but there is no complete, local, and effective decision-making support system. The water inrush in the mine is large, which affects the normal operation of the mine and the stability of the mine.

This paper studies the whole process of water inrush and water diversion in aquifer fault roadway of underground engineering and analyzes the mechanism of water inrush disaster. Establishing a two-dimensional model under Darcy's law to analyze the change of stress and water flow velocity in fault roadway during a water inrush disaster, the disaster of water inrush in the rock under different working conditions, considers the mutual coupling between solid and liquid, and studies the rock and water layer based on fluid-structure coupling.

Through model simulation, the data results can forecast the amount of water inrush from the fault and the pressure on the engineering roadway when water inrush occurs. In view of the increasingly serious problem of fault water inrush, to reveal the fluid-structure coupling effect of fault water inrush at different times and stages, a non-Darcy fluid model is adopted, and factors such as stress and pore water pressure are introduced into the fracture area. With COMSOL software, non-Darcy free flow equations are established before and after the three-stage fracture conduction, and the mechanism of water inrush and seepage the action of stress water pressure are obtained. Through the numerical calculation of COMSOL software, a two-dimensional numerical model is established to analyze the water transmission variation law of related fault water inrush and study the water transmission process of fault water inrush. The finite element analysis software such as COMSOL is used for numerical simulation and calculation to study the water inrush process in the fault, and the numerical analysis method is used for research.

2. Darcy's Law and Fluid-Structure Coupling

2.1. Derivation Formula of Darcy's Law. If the compressive stress (strain) is positive, then at the initial stage of stress, as the porous medium is still in the elastic stage, according to relevant experience and generalized Hooke's law, the displacement of the porous medium and the pressure of the fluid interact, and the relationship can be expressed by referring to the following expression:

$$Gu_{i,jj} + \frac{G}{1-2\nu} u_{k,kj} - \alpha p_{,i} + F_i = 0, \tag{1}$$

where G is the shear modulus of the rock, p is the porous pressure, ν is the Poisson's ratio, F_i is the component of the force, and u_i is the component of the displacement. α is the Biot coefficient, and the specific value depends on the compressibility of the rock composition.

The precondition for the use of Darcy's law in this model is to regard the pores as saturated. Then, according to its fluid-related mass conservation equation substituted into Darcy's law, it can be concluded that

$$-c_1\left(\frac{\partial \varepsilon_v}{\partial t}\right) + c_2\left(\frac{\partial p}{\partial t}\right) = \nabla \cdot [k(\nabla p + \rho_1 g \nabla z)], \tag{2}$$

where ρ_1 is fluid density (kg/m^3), and g is gravitational acceleration (m/s^2). The values of c_1 and c_2 are listed in

$$\begin{aligned} c_1 &= 1 - \frac{K}{K_s} = \frac{3(\nu_u - \nu)}{B(1+\nu_u)(1-2\nu)}, \\ c_2 &= \frac{\varphi}{\beta_1} + \frac{1-\varphi}{K_s} = \frac{9(1-2\nu_u)(\nu_u - \nu)}{2GB^2(1-2\nu)(1+\nu_u)}, \end{aligned} \tag{3}$$

where φ is the porosity of the rock, B is the Skempton coefficient, β_1 is the bulk modulus of the fluid in the pores (Pa), ν_u is the Poisson's ratio of the solid in the rock, ν is the Poisson's ratio of the rock, K is the bulk modulus of the rock, Ks is the bulk modulus of the rock grains, and t is the time (s).

2.2. Boundary Conditions of Darcy's Law. For the model setting and actual construction, the following points are simplified: (1) Without reference to the effect between adjacent rock layers, the same rock layer is regarded as homogeneous and isotropic material. (2) The tectonic stress caused by geological tectonic movement is not considered. (3) For the rock mass before excavation, the cracks of the rock are ignored, and the small differences between different rocks are not considered. The simplified rock parameters are regarded as the overall impermeable environment. (4) The movement of water in the aquifer conforms to Darcy's law.

This study presents the construction of a Darcy's law model, which involves applying pressure on both sides of the aquifer and ensuring continuous boundary conditions between the fault and the aquifer, impermeable rock layer, and roadway. To prevent water from flowing into the rock layer, the upper and lower boundaries of the aquifer, as well as the boundary between the fault zone and the rock layer, are set to zero flow. Meanwhile, the boundary between the fault zone and the road is determined by the water pressure. These carefully crafted boundary conditions and considerations would provide more accurate predictions for the potential occurrence of water inrush from faults in underground engineering projects.

2.3. Calculation Formula of Fluid-Structure Coupling. On the basis of the established Darcy model, the plane stress field in structural mechanics is superimposed. A numerical simulation of fluid-solid coupling is carried out. This method can be used to simulate the failure mechanism of rock and the change of rock properties under water flow scouring. In this case, the model can also calculate the flow of fluid in this case.

$$\varphi = (\varphi_0 - \varphi_r) \exp\left(-\alpha_\varphi \cdot \sigma_v\right) + \varphi_r, \tag{4}$$

where ϕ_0 refers to the porosity of rock under zero-stress state, and α_ϕ refers to the stress sensitivity coefficient of pores. ϕ_r is the porosity of rock under high-stress compression, which will not be considered temporarily in this experiment. σ_v refers to the average effective stress (take the direction of tensile stress as the positive direction). The value of average effective stress σ_v can be calculated by the following formula:

$$\sigma_v = \frac{(\sigma_1 + \sigma_2 + \sigma_3)}{3} - \alpha P, \tag{5}$$

where α is the elastic porosity coefficient, which can be calculated by the formula (1). The specific value depends on the compressibility of the medium composition, and σ_1, σ_2, and σ_3 are the three principal stresses of the element. In addition, it can also be approximately considered that the relationship between porosity and permeability is as follows:

$$K = K_0\left(\frac{\varphi}{\varphi_0}\right)^3, \tag{6}$$

where K_0 refers to the permeability of rock under zero-stress conditions (m^2), and K refers to the permeability of rock under stress conditions (m^2).

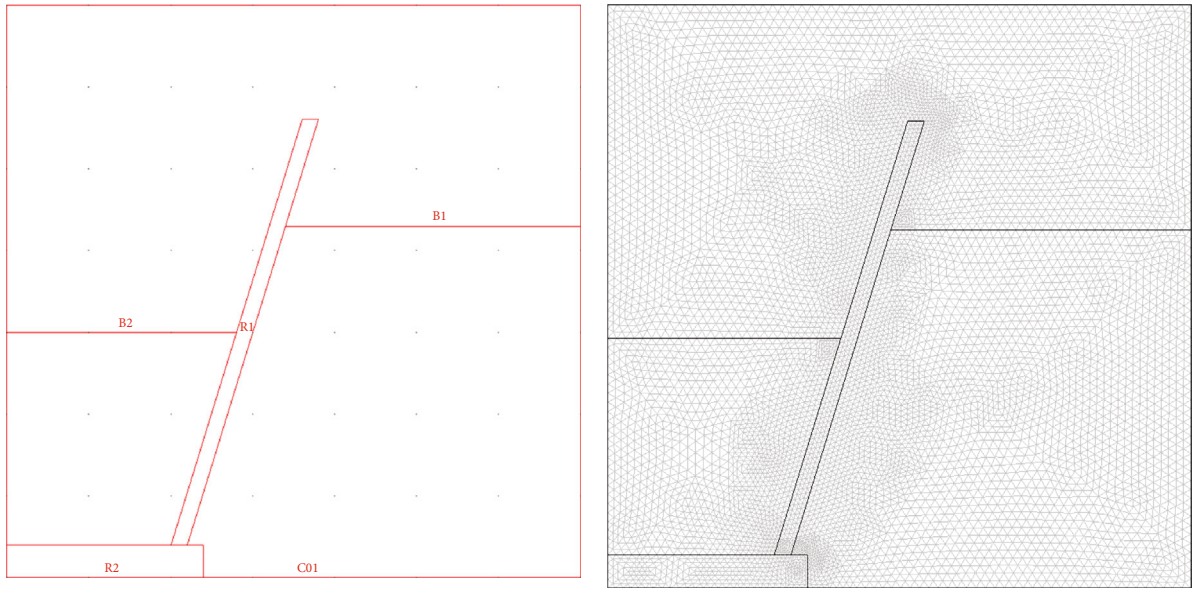

(a) Geometric model (b) Meshing of geometric model

Figure 1: Geometric model.

On the basis of Darcy's law model, body load is applied to the aquifer and fault zone areas and damping is applied. The upper boundary of the aquifer and the lower boundary of the model area constrain the displacement, and the two sides of the aquifer and the model area constrain the displacement in the x direction.

3. Model Establishment and Working Condition Setting

3.1. Establishment of the Geometric Model. Based on geological, geomechanics, and hydrogeological data, a simple geometric model containing faults is constructed according to plane strain conditions. As shown in Figure 1, the model is 350 m long and 350 m high. The aquifer is above, the roadway is at the lower left corner, and the coordinates of the fault zone are (100 m and 20 m), (110 m and 20 m), (180 m and 280 m), and (190 m and 280 m). The water flows from the aquifer to the roadway through the fault zone. Other formation conditions are set as impermeable formations.

3.2. Setting of the Solution Domain. Figure 2 shows the setting of the solution domain.

3.3. Setting of Model Constants. For the conditions of the model and the related influencing conditions of Darcy's law and the plane stress field, the constants shown in Table 1 are established according to the model and research purpose.

3.4. Setting of Working Conditions

3.4.1. Working Conditions of Darcy's Law Seepage Model

(1) The test was divided into 5 groups by aquifer pressure. The corresponding pressure cloud chart, velocity cloud chart, and broken line diagram for different aquifer pressures are drawn

(2) By changing the permeability of fault zones, the initial permeability of fault zones was set under different working conditions as $1 \times 10^{-12}\,m^2$, $1 \times 10^{-13}\,m^2$, $1 \times 10^{-14}\,m^2$, $1 \times 10^{-15}\,m^2$, and $1 \times 10^{-16}\,m^2$. And the corresponding pressure cloud chart, velocity cloud chart and line chart under different permeabilities are drawn

(3) The ratio K of fracture zone permeability to aquifer permeability changed and was set to $K = 0.01$, $K = 0.1$, $K = 1$, $K = 10$, $K = 100$, and $K = 1000$, respectively. Draw the corresponding pressure cloud picture, velocity cloud picture, and corresponding line chart at different ratios K

(4) We use COMSOL to simulate the occurrence of water inrush, select several representative transient times, and draw a pressure nephogram, velocity nephogram, and corresponding broken line graph of the model at different times

3.4.2. Working Conditions of Fluid-Solid Coupling Model

(1) The initial pressure of the aquifer was varied and divided into five groups: 2 MPa, 8 MPa, 14 MPa, 15 MPa, and 25 MPa. The corresponding pressure and velocity contour plots were then generated for each group, demonstrating the effects of varying aquifer pressures

(2) The ratio K of fracture zone permeability to aquifer permeability varied and was set at K values of 0.01, 0.1, 1, 10, 100, and 1000, respectively. The corresponding pressure and velocity contour plots, as well

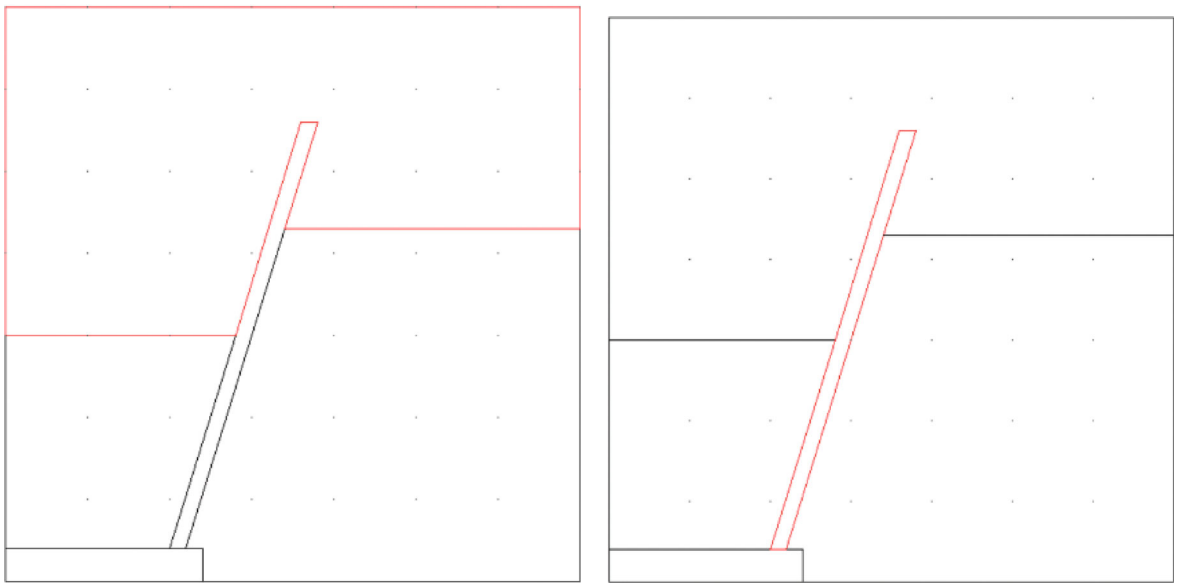

(a) Aquifer (b) Fault zone

Figure 2: Setting of the solution domain.

as line graphs, were generated for each K value to illustrate the effects of varying K ratios

(3) The stress sensitivity coefficients of the pores in the fault zone are 5×10^{-8} Pa^{-1}, 6×10^{-8} Pa^{-1}, 7×10^{-8} Pa^{-1}, 8×10^{-8} Pa^{-1}, and 9×10^{-8} Pa^{-1}, respectively. Pressure and velocity contour plots as well as line graphs were generated to illustrate the effects of varying permeability, showing corresponding changes in pressure and velocity

4. Numerical Simulation Results

4.1. Working Condition Analysis of Single Seepage Field

4.1.1. Analysis of Seepage Law of Initial Pressure in Different Aquifers. Different working conditions for the fault model were established based on the specified solution domain and boundary conditions of the Darcy field, including varying the initial pressure of the aquifer at 2 MPa, 4 MPa, 6 MPa, 8 MPa, and 10 MPa. By simulating fault water inrush under these conditions using the software, various scenarios were generated and visualized in Figures 3 and 17 in the Appendix.

The line graph depicted in Figure 4 corresponds to the following section line coordinates: for the aquifer, (0 m and 160 m) and (150 m and 160 m); for the fault zone, (150 m and 160 m) and (105 m and 20 m).

It can be seen from the pressure diagram that the pressure changes continuously along the aquifer and fault zone. The overall pressure change is that the pressure value decreases gradually from the aquifer to the fault zone to the roadway. The pressure on each area varies with the initial pressure value of the aquifer at the same location. The same change rule of each region is that as the aquifer pressure increases, the corresponding pressure of the region also increases. Different regions have different ranges of change. By comparing the pressure change chart, the initial pressure of the aquifer under different restrictive conditions increases, the color segmentation distribution of the pressure cloud chart becomes more and more obvious, and the pressure span also gradually increases. The area with obvious pressure changes mainly occurs in the area with continuous aquifers and fault zones.

The velocity of fault fluid increases as the initial pressure of the aquifer is raised across various working conditions. However, there is a sudden change in the velocity values observed within the fault zone. When fluid flows from the aquifer into the fault zone, the velocity of the area connected to the deeper side of the aquifer increases suddenly and then decreases before flowing into the roadway.

Table 1: Constant table of fault water inrush model.

Name	Expression
ν_m	0.3
p_i	6.2e6
k	1e-3
g	9.8 (m^2)
Water density: rho	1000 (kg/m^3)
Water pressure: p_1	5e6 (pa)
Fault zone water pressure: Pa	0.1e6 (pa)
Permeability of aquifer: Kd	1.9e-8 (m^2)
Dynamic viscosity coefficient: p_s	0.001 ($pa \times s$)
Length of the model: b	350 (m)
Initial pressure: P_1	$10 \times 1e6$ (pa)
Young's modulus: Ee	2.713*e*9 (pa)
Es	8.139e9 (pa)
Poisson coefficient: *Mu*	0.339
Density	1250 (kg/m^3)

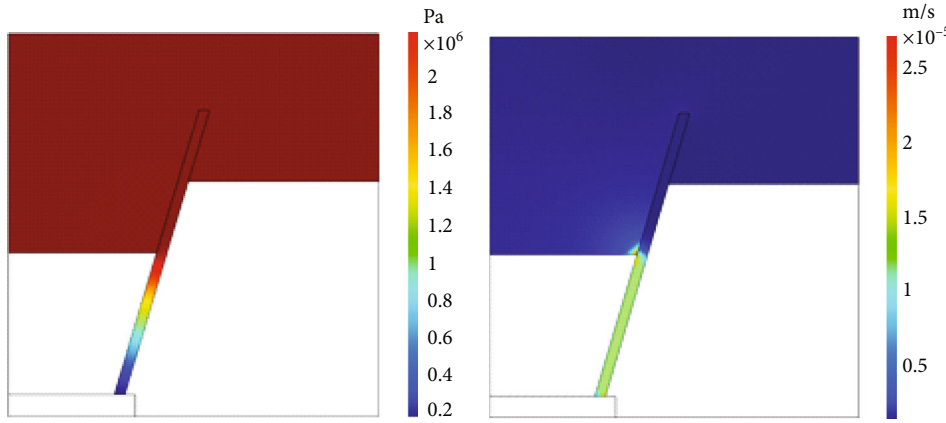

(a) Pressure cloud chart of 2 MPa (b) Velocity cloud chart of 2 MPa

Figure 3: Cloud images of pressure and velocity of faults under different aquifer pressures.

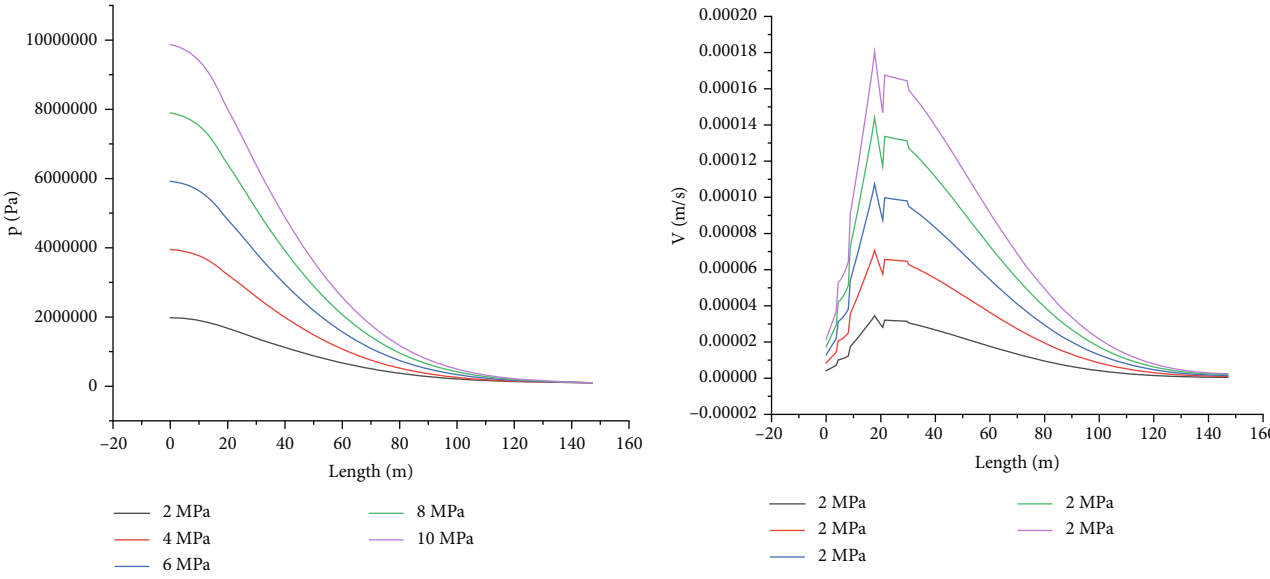

(a) Pressure diagram (b) Velocity diagram

Figure 4: Initial pressure of different aquifers.

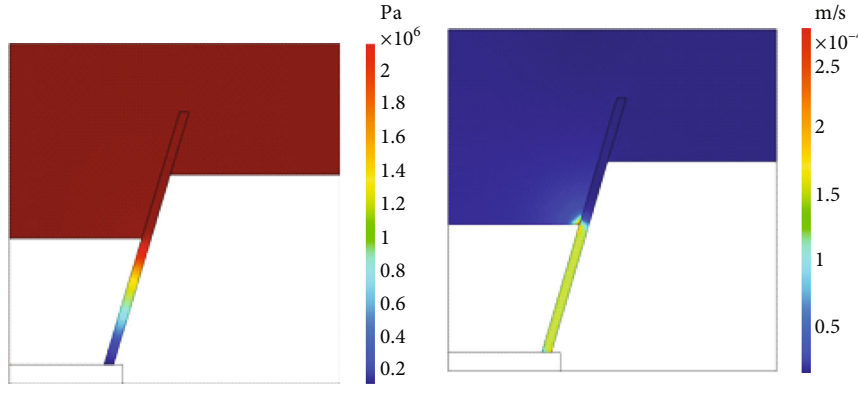

(a) Permeability 1×10^{-11} m^2 (b) Permeability 1×10^{-11} m^2

Figure 5: Cloud chart of pressure and velocity under different fracture zone permeability.

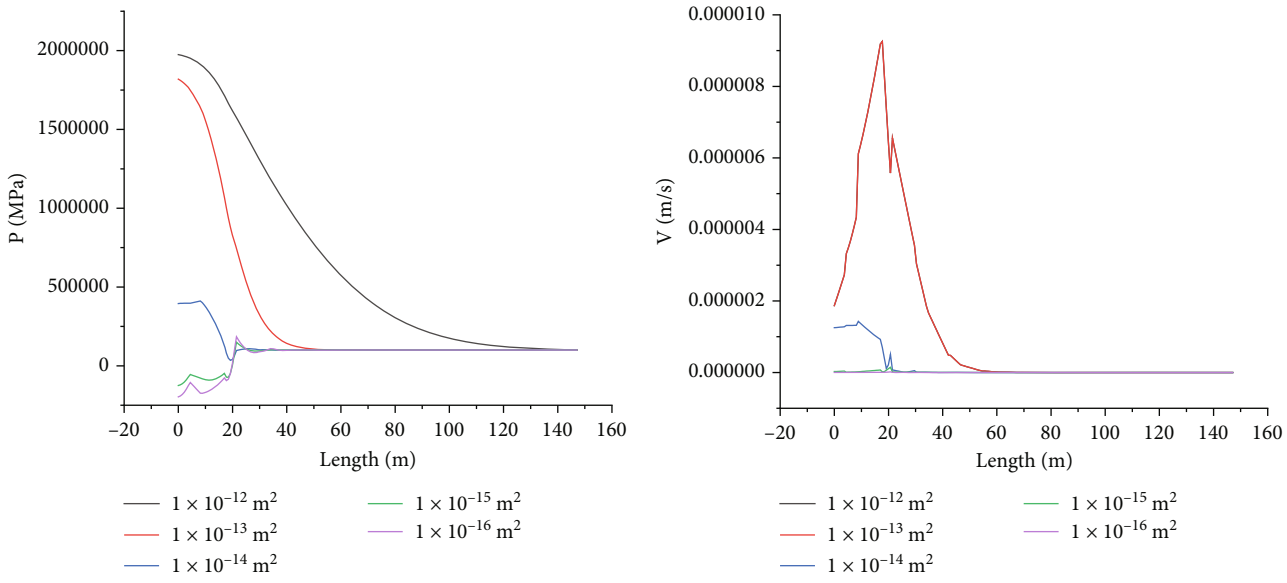

(a) Pressure diagram (b) Velocity diagram

Figure 6: Permeability map of different fault zones.

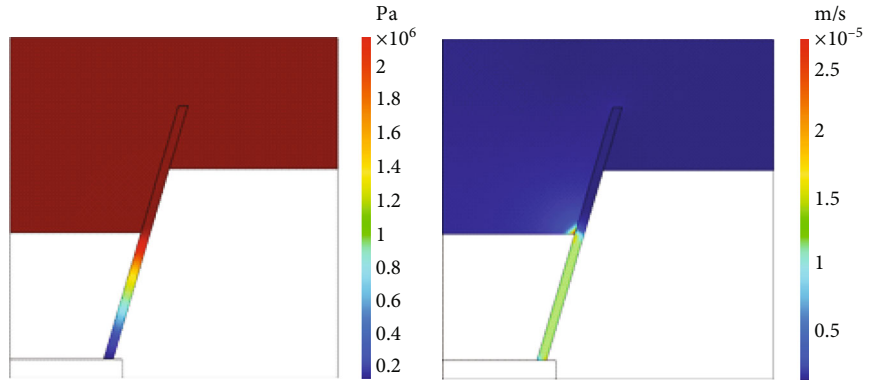

(a) Pressure cloud chart of $K = 0.01$ (b) Velocity cloud chart of $K = 0.01$

Figure 7: Pressure and velocity cloud chart of fault in different proportions of fracture zone permeability and aquifer permeability.

According to the line diagram, with the increase of aquifer pressure, the fault zone pressure and water inrush speed increase. There is a sudden change in the value of the velocity curve from the fault zone to the roadway.

According to the above analysis, if there is water inrush from faults in underground works, the initial pressure of the aquifer will affect the pressure and speed of water inrush, which is an important influencing factor. With the increase of initial pressure of aquifers under different working conditions, the peak value of fluid pressure and fluid velocity in the corresponding fault zone is larger, and the possibility of water inrush accidents is also greater. Therefore, during the excavation of underground works with faults, if there is an aquifer in the section, the initial pressure of the aquifer shall be determined in time when the water inrush is determined in advance. When the underground excavation project is close to the fault water-bearing area, the water exploration must be carried out, and the method of simultaneous exploration and excavation shall be adopted.

To reduce the risk of water inrush disasters caused by excessive aquifer pressure, the following methods can be adopted: (1) Lower the aquifer water level to decrease aquifer pressure once the elevation of the working face has been determined for safe production. Water can be partially or completely drained. (2) In case of high initial aquifer pressure, groundwater can be blocked off either temporarily or permanently by building an impermeable gate. (3) Grouting technology can be employed to inject cement into stratum holes, enabling diffusion, solidification, and hardness. This technique not only prevents groundwater but also strengthens the rock. Furthermore, an efficient drainage system is critically important for prompt draining and rescue operations after a water inrush disaster. The supporting drainage pipeline, water pump, and power supply system must be checked frequently.

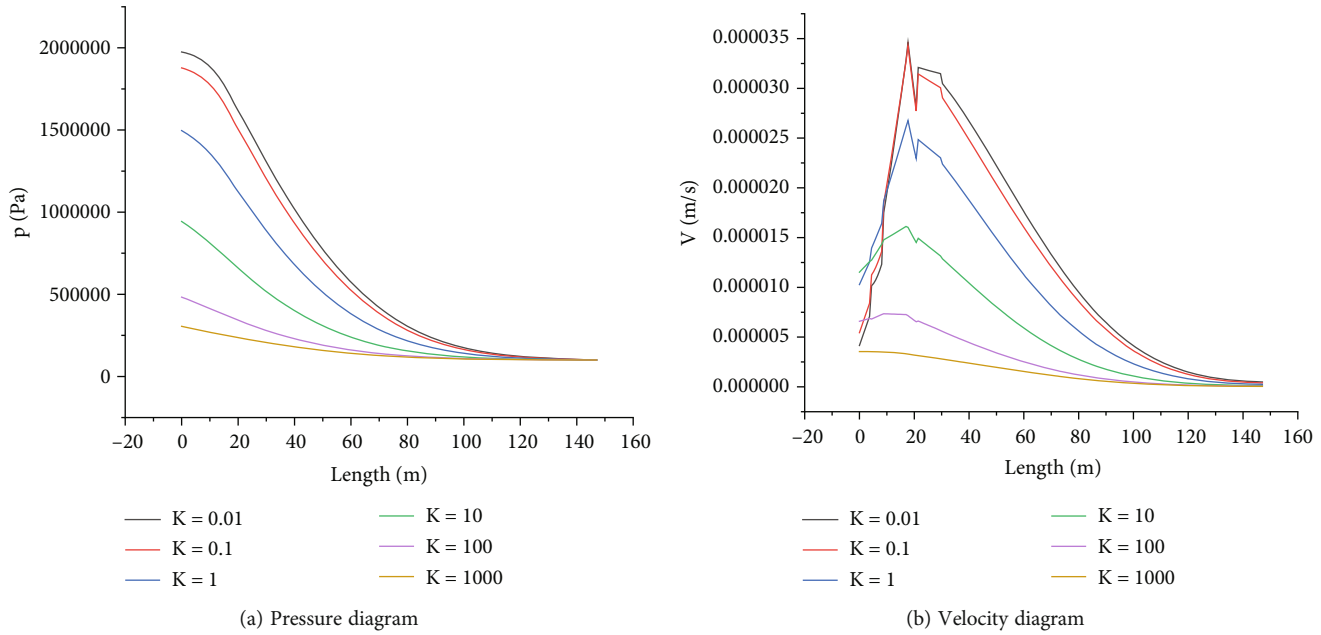

(a) Pressure diagram (b) Velocity diagram

Figure 8: Fracture zones with different proportions and aquifer permeability.

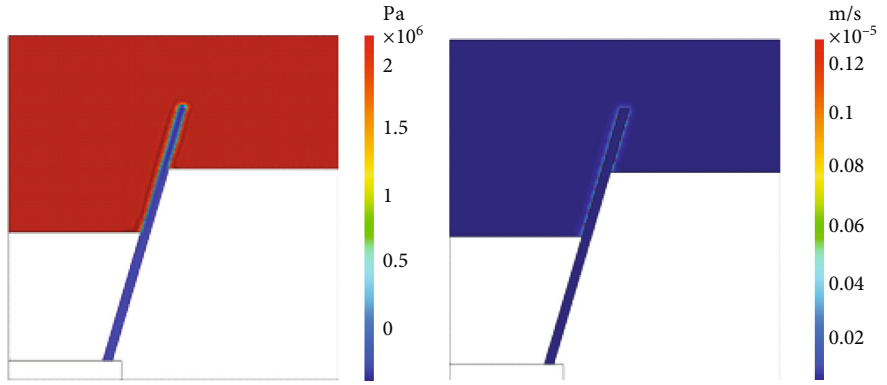

(a) Pressure cloud chart of 1 s (b) Velocity cloud chart of 1 s

Figure 9: Pressure and velocity cloud chart of fault under different transient conditions.

4.1.2. Analysis of Seepage Law of Permeability in Different Fault Zones. The permeability of the fault zone changed and was set under different working conditions as 1×10^{-12} m^2, 1×10^{-13} m^2, 1×10^{-14} m^2, 1×10^{-15} m^2, and 1×10^{-16} m^2. The pressure contour plots, as well as the velocity contour plots and their corresponding line graphs, are drawn in Figures 5, 18 in the Appendix, and 6 under different levels of permeability. Under the conditions of different fracture zone permeability, the specific changes of the corresponding pressure and velocity cloud chart of the fault, and the corresponding pressure and velocity line graphs are drawn through the obtained pressure and velocity cloud chart to summarize the seepage laws of the corresponding fault.

As illustrated by the pressure cloud chart, the maximum pressure of different fault zones tends to increase as their permeability decreases. This is due to the fact that, as the permeability of the fault layer dwindles, the pressure value of the fault zone rises under the pressure of the aquifer. However, when the fault permeability has decreased to a certain extent, water inrush becomes unlikely. This is because, even though the aquifer still seeks to flow due to the pressure gradient, the permeability of the fault zone is insufficient to allow sizable water flow and consequential water pressure into the roadway, thereby averting water inrush.

According to the velocity cloud chart, when the permeability of the fault zone reaches a certain value, the velocity remains relatively constant, and the water flow rate from the aquifer through the fault and into the roadway becomes small, which in turn reduces the likelihood of water inrush. Consequently, increasing the permeability of the fault fracture zone to such stable levels with low water flow speeds will result in slow water flow into the roadway, minimizing the risk of disaster.

Based on the pressure line diagram, the limit is found to be 1×10^{-14} m^2. When permeability increases, the pressure transmitted from the aquifer to the roadway increases accordingly. Conversely, when the permeability decreases,

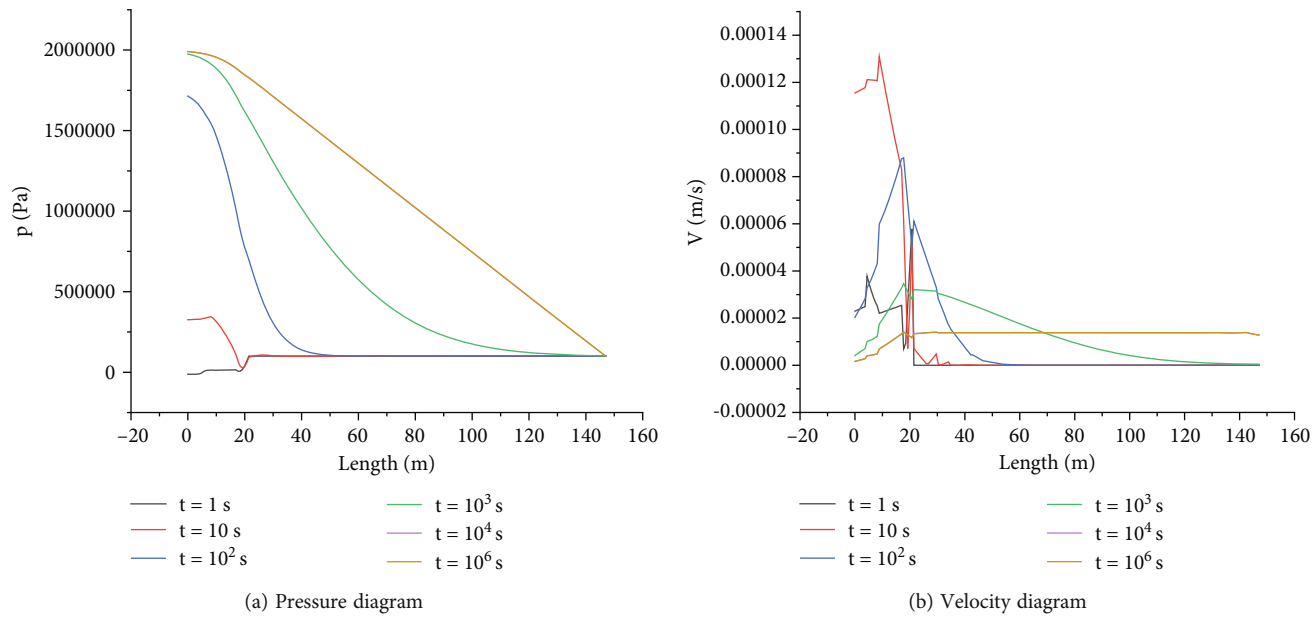

(a) Pressure diagram (b) Velocity diagram

Figure 10: Different times under the same working condition.

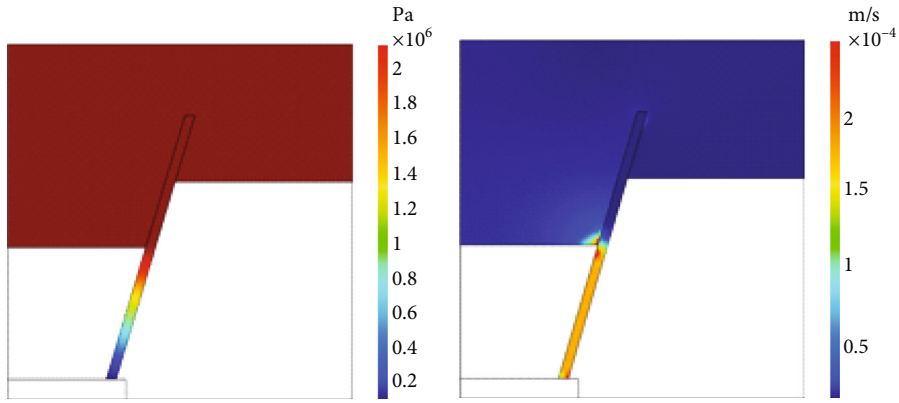

(a) Pressure cloud chart of 2 MPa (b) Velocity cloud chart of 2 MPa

Figure 11: Pressure and velocity cloud chart of fault under different aquifer pressures.

the pressure transmitted from the aquifer to the roadway decreases as well. The velocity line graph, on the other hand, shows that as the permeability of the fault zone increases, the velocity changes more rapidly and the curve becomes more pronounced. There is an abrupt increase in velocity at the joint of the fault zone and the roadway. This sudden change in velocity is due to the pressure boost caused by the water section becoming smaller.

After analyzing the pressure line diagram, we have determined that the permeability of the fault zone has a significant impact on the pressure transmitted to the roadway. In particular, as permeability increases, the pressure transmitted from the aquifer to the roadway also increases, creating potential risks for engineering structures. Therefore, efforts should be made to monitor and control the permeability of the fault zone in order to ensure the safety and stability of the roadway. In addition to pressure, the velocity line graph also provides valuable insights into the behavior of the aquifer-fault zone system. As the permeability of the fault zone increases, the velocity changes more rapidly, indicating a greater flow of water through the system. Furthermore, the curve of the velocity graph becomes more pronounced, suggesting that the flow becomes more concentrated and potentially turbulent.

4.1.3. Analysis of Seepage Law of Different Fracture Zone and Aquifer Permeability Ratio. The permeability of the aquifer is set at K_2, and the permeability of the fault zone formed by the fault is set at K_1. For ease of representation, it is set as $K = K_1/K_2$. The working condition is set to $K = 0.01$; $K = 0.1$; $K = 1$; $K = 10$; $K = 100$; and $K = 1000$.

According to the analysis of the cloud charts in Figures 7, 19 in the Appendix, and 8, the permeability ratio of the aquifer and fault zone is a significant influencing factor of water inrush. When comparing the pressure cloud chart, it can be observed that when the permeability ratio

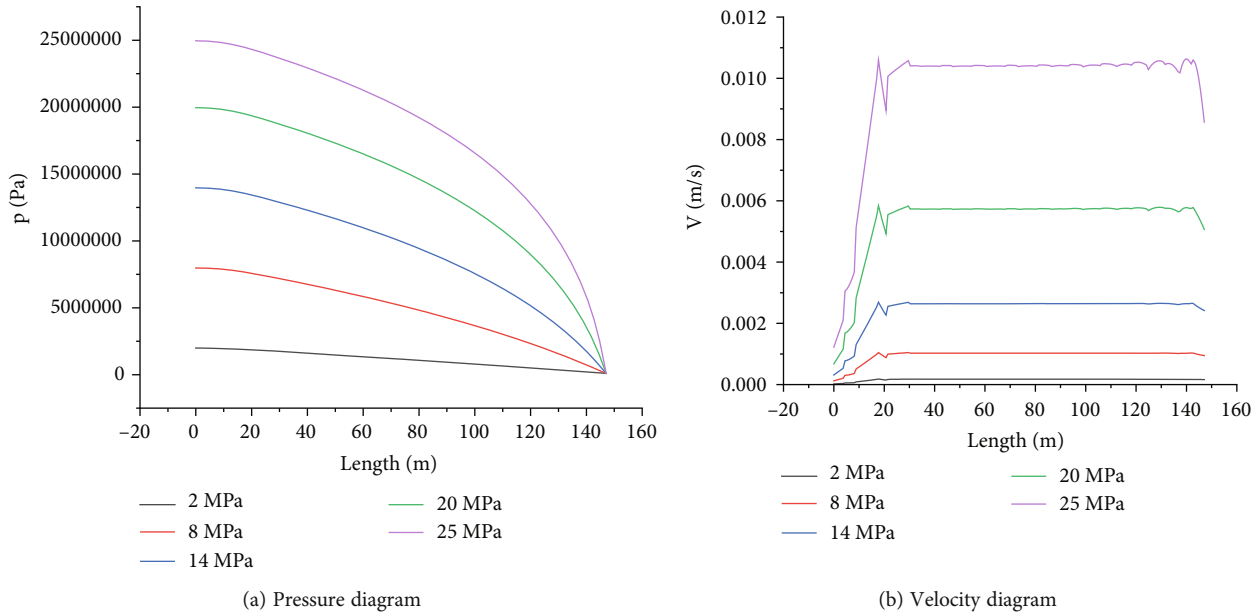

(a) Pressure diagram (b) Velocity diagram

Figure 12: Initial pressure of different aquifers.

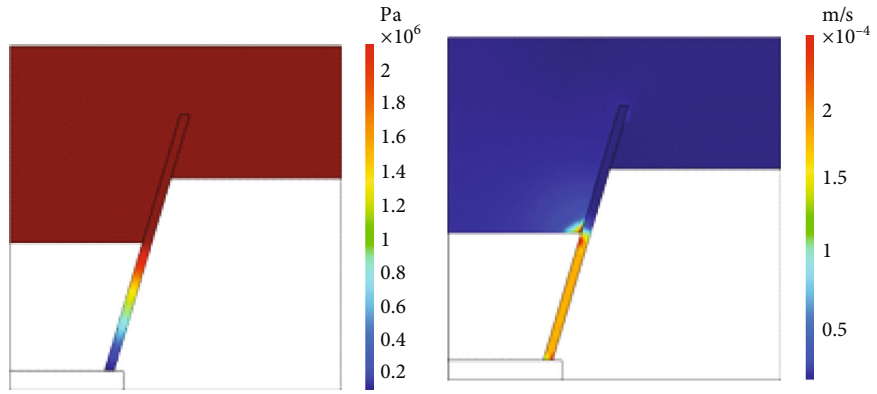

(a) Pressure cloud chart of $K = 0.01$ (b) Velocity cloud chart of $K = 0.01$

Figure 13: Pressure and velocity cloud chart of fault in different proportions of fracture zone permeability and aquifer permeability.

of the fault zone to the aquifer is high, the specific pressure of the fault zone is smaller than that of the aquifer, which results in a lower possibility of water inrush disaster. It results in less water pressure being transmitted from the fault zone to the roadway. Therefore, a large permeability ratio of the aquifer to the fault zone implies that there is less likelihood of water inrush disasters. When the permeability ratio of the aquifer to the fault zone decreases, the pressure of the fault zone first increases and then decreases. When the permeability of the fault zone is much larger than that of the aquifer, water inrush is not likely to occur.

By comparing the velocity cloud chart, it is not hard to find that with the decrease in the ratio of the permeability of the fault zone to the permeability of the aquifer, the velocity cloud chart of the fault zone suddenly increases at the joint of the deep side of the aquifer and the aquifer, resulting in water inrush. However, as the permeability ratio of the aquifer and fault zone decreases again, the speed gradually slows down. It can be seen from the line diagram that at the intersection of the roadway and the fault zone, the pressure and speed change suddenly, the pressure decreases suddenly, and the water flow speed increases rapidly, which are the reasons for the roadway water inrush accident. If the underground project contains water inrush from faults, the permeability ratio of the aquifer to the fault zone will affect the pressure and speed of water inrush, which is an important influencing factor. For avoiding or reducing the occurrence of water inrush disasters, the permeability ratio of the controlled aquifer and the fault zone is large or small, that is, the greater the difference between the permeability of the two, the more difficult the water inrush will occur.

4.1.4. Analysis of Seepage Law of Fault under Different Transient Conditions. Setting the permeability of the fault zone at $k = 10^{-12}\,\mathrm{m}^2$ and the initial pressure of the aquifer at 2 MPa, we investigate various transient conditions and present the corresponding pressure, velocity cloud chart, and line graph changes.

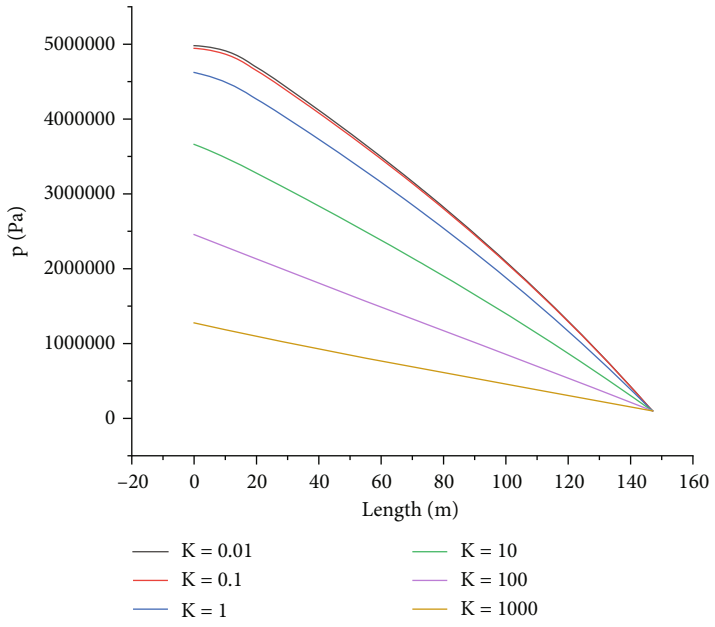

(a) Pressure diagram

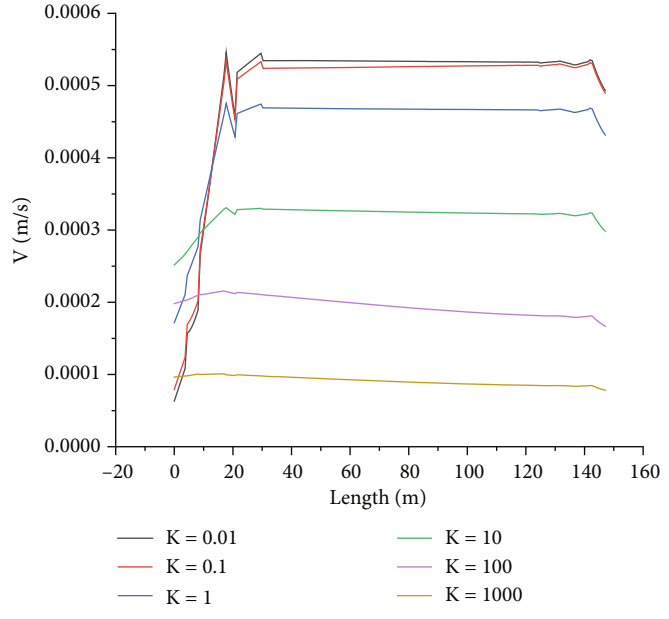

(b) Velocity diagram

Figure 14: Fracture zones with different proportions and aquifer permeability.

According to the water inrush animation of the COMSOL multiphysics model, combined with Figures 9, 20 in the Appendix, and 10, it can be found that the water inrush occurs for a certain time and then gradually becomes stable. When the time reaches 10^3 s, the pressure of the aquifer on the fault zone increases, and the flow rate of the water in the fault zone gradually increase, causing the accident of water inrush.

The disaster of water inrush does not happen suddenly at a certain moment as observed by the naked eye. It is the continuous accumulation of the pressure of the aquifer on the fault zone over a period. With the variety of time, the pressure is accumulated to an unbearable pressure. With the increase of time, the water flow speed also increases, reaching a peak value. Although the fluid speed starts to decline after reaching the peak value, it still maintains a high-speed movement state along the direction from the fault zone to the roadway. Finally, when it reaches the intersection of the fault zone and the roadway, the water flows into the roadway, forming a serious water inrush disaster.

4.2. Analysis of Fluid-Structure Coupling Working Condition

4.2.1. Fluid-Structure Coupling Analysis of Faults under Different Aquifer Pressures. As shown in Figures 11 and 21

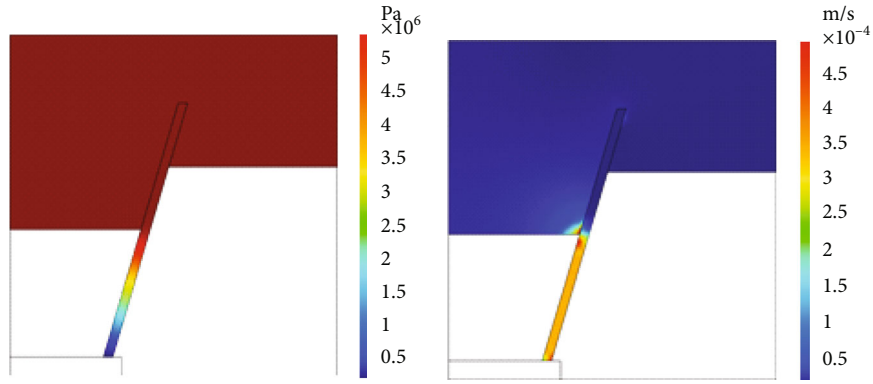

(a) Pressure cloud chart with 5×10^{-8} Pa^{-1} (b) Velocity cloud chart with 5×10^{-8} Pa^{-1}

Figure 15: Pressure and velocity cloud chart under different stress sensitivity coefficients.

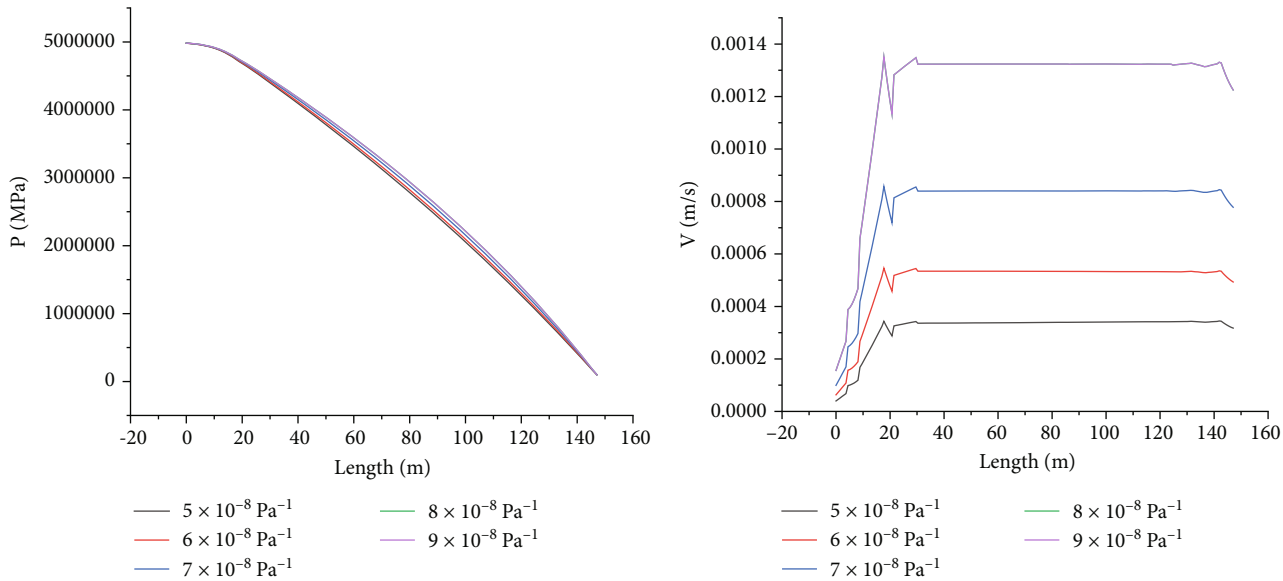

(a) Pressure diagram (b) Velocity diagram

Figure 16: Different stress sensitivity coefficients.

in the Appendix, a comparison of the pressure cloud chart indicates that the maximum value of pressure increases continuously with the initial pressure of the aquifer, while the pressure distribution remains largely unchanged. Similarly, a comparison of the velocity cloud chart reveals that the increase in velocity is more prominent as the aquifer pressure increases. Notably, after the aquifer water rushes into the fault zone, velocity continues to increase as the fault zone approaches the roadway. Our observations underscore the importance of accounting for aquifer pressure in subsurface reservoir management. Additionally, these findings could help inform strategies to mitigate potential hazards associated with fault zones and fluid flow dynamics. Further research is warranted to probe this complex problem in greater detail.

The pressure line diagram in Figure 12 demonstrates that an increase in initial aquifer pressure does not lead to sudden changes in fracture behavior. Meanwhile, the velocity line shows a sharp increase in velocity at the fault-coal roadway junction and a generally positive correlation between peak velocity and initial aquifer pressure. In contrast, velocity within the fracture remains relatively stable. The results suggest that variations in initial aquifer pressure may play a critical role in determining fluid flow dynamics near fault zones. However, further research is needed to fully characterize the complex interplay among fracture behavior, velocity dynamics, and aquifer pressure. These findings could have important implications for subterranean reservoir management and development.

4.2.2. Fluid Solid Coupling Analysis of Fracture Zone and Aquifer Permeability with Different Proportions. The permeability of the aquifer is set at K_2, and the permeability of the fault zone formed by the fault is set as K_1. For ease of representation, it is set as $K = K_1/K_2$.

The working condition is set to $K = 0.01$; $K = 0.1$; $K = 1$; $K = 10$; and $K = 100$; $K = 1000$.

Analyzing Figures 13 and 22 in the Appendix, we can see in the pressure cloud chart that as the permeability ratio increases, the color distribution becomes increasingly

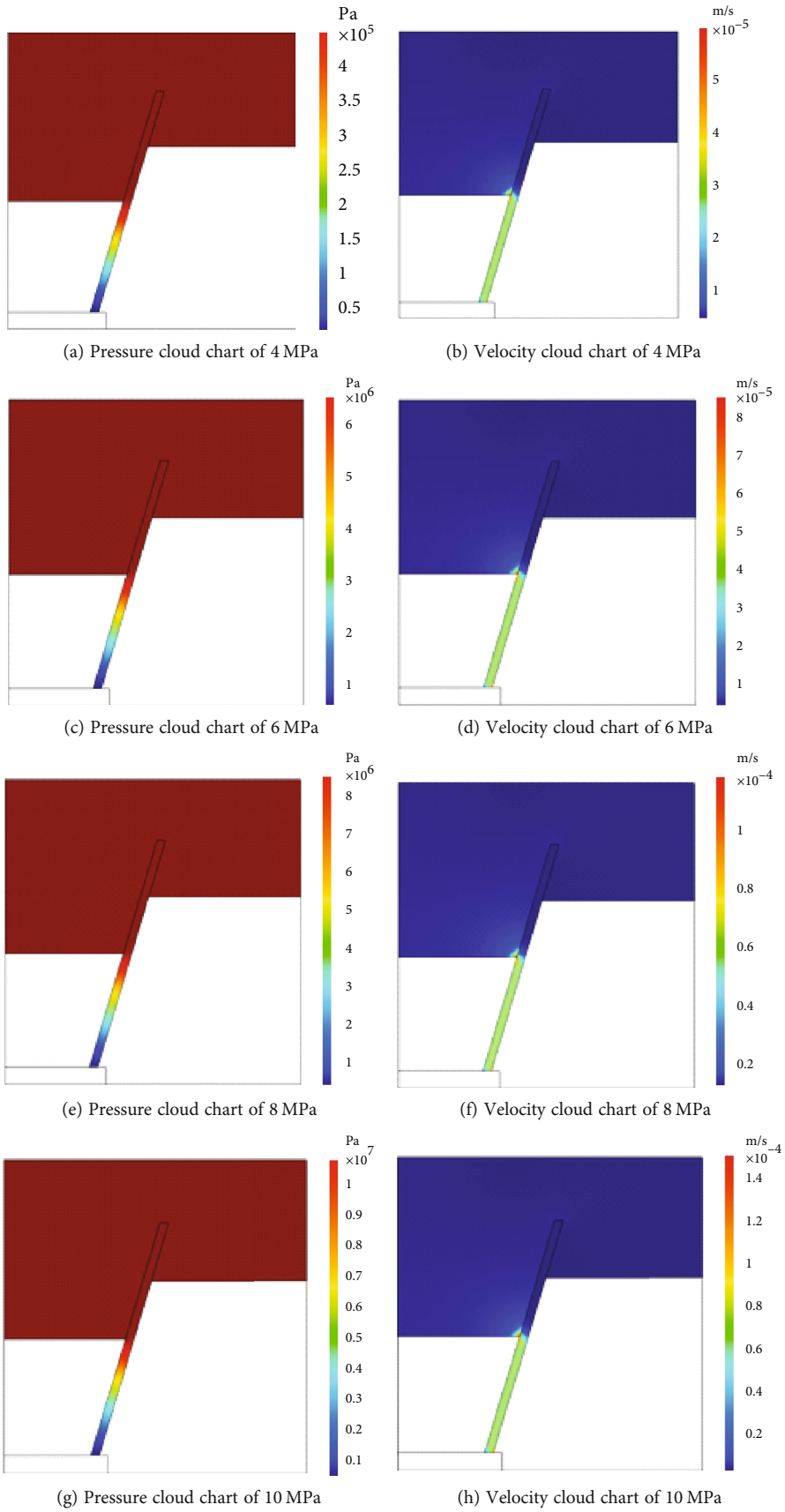

(a) Pressure cloud chart of 4 MPa

(b) Velocity cloud chart of 4 MPa

(c) Pressure cloud chart of 6 MPa

(d) Velocity cloud chart of 6 MPa

(e) Pressure cloud chart of 8 MPa

(f) Velocity cloud chart of 8 MPa

(g) Pressure cloud chart of 10 MPa

(h) Velocity cloud chart of 10 MPa

Figure 17: Cloud images of pressure and velocity of faults under different aquifer pressures.

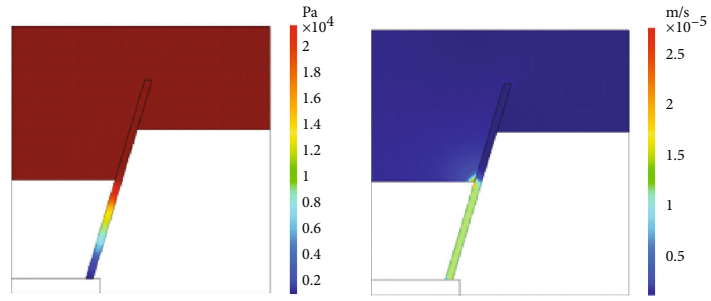

(a) Pressure cloud chart of 1×10^{-12} m^2 (b) Velocity cloud chart of 1×10^{-12} m^2

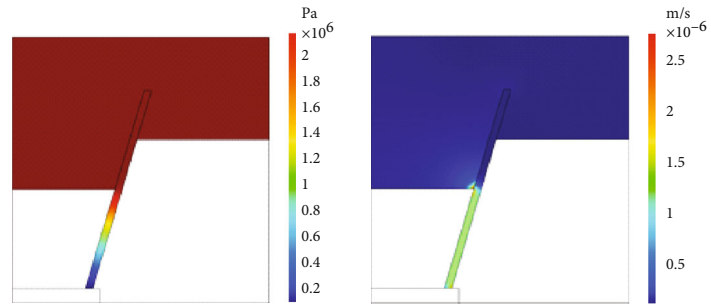

(c) Pressure cloud chart of 1×10^{-13} m^2 (d) Velocity cloud chart of 1×10^{-13} m^2

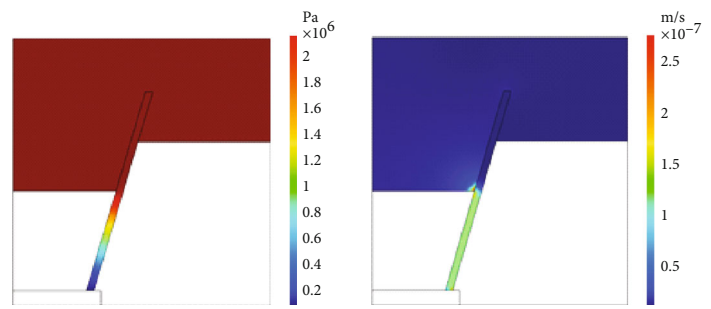

(e) Pressure cloud chart of 1×10^{-14} m^2 (f) Velocity cloud chart of 1×10^{-14} m^2

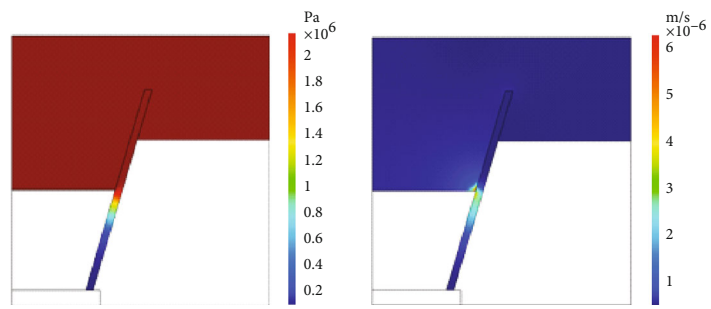

(g) Pressure cloud chart of 1×10^{-15} m^2 (h) Velocity cloud chart of 1×10^{-15} m^2

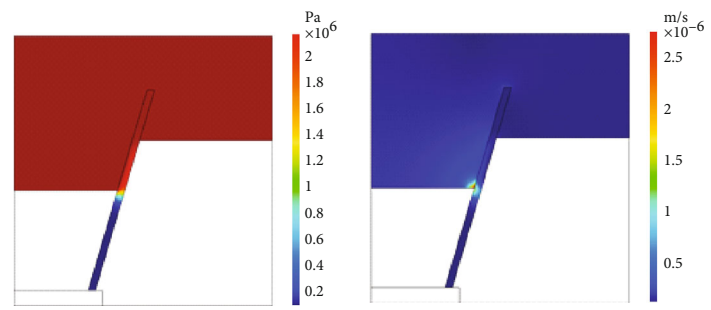

(i) Pressure cloud chart of 1×10^{-16} m^2 (j) Velocity cloud chart of 1×10^{-16} m^2

Figure 18: Cloud chart of pressure and velocity under different fracture zone permeability.

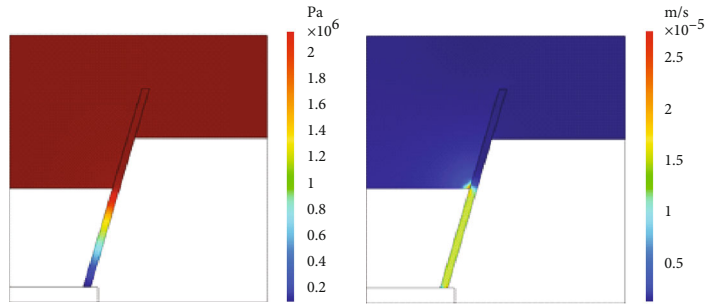

(a) Pressure cloud chart of $K = 0.1$ (b) Velocity cloud chart of $K = 0.1$

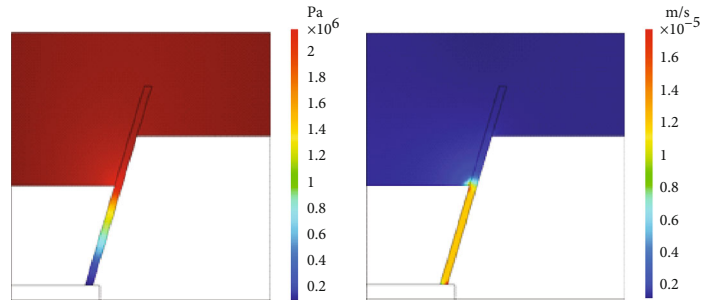

(c) Pressure cloud chart of $K = 1$ (d) Velocity cloud chart of $K = 1$

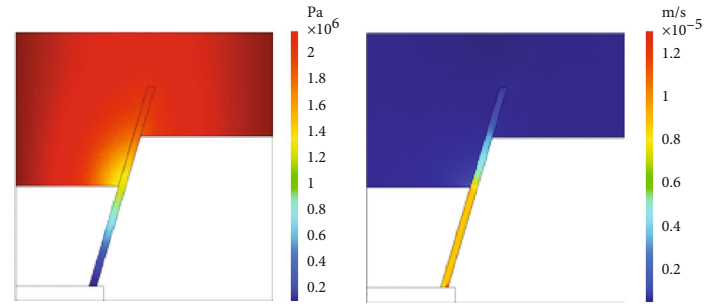

(e) Pressure cloud chart of $K = 10$ (f) Velocity cloud chart of $K = 10$

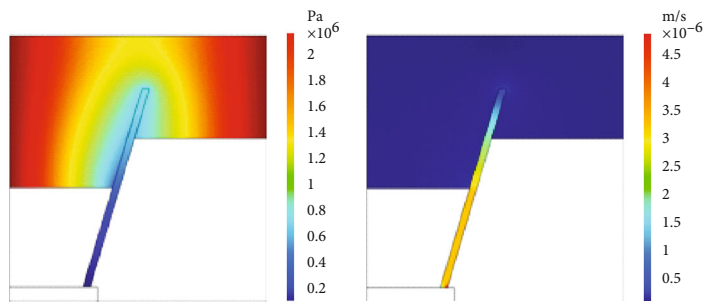

(g) Pressure cloud chart of $K = 100$ (h) Velocity cloud chart of $K = 100$

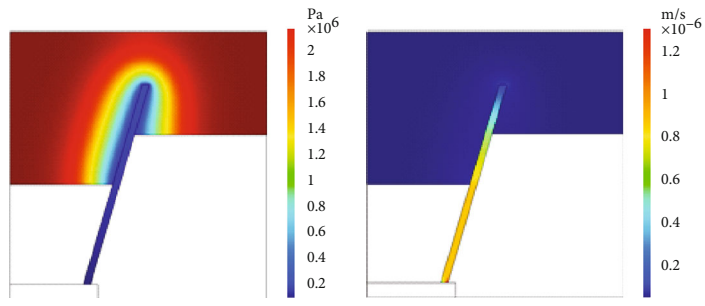

(i) Pressure cloud chart of $K = 1000$ (j) Velocity cloud chart of $K = 1000$

FIGURE 19: Pressure and velocity cloud chart of fault in different proportion of fracture zone permeability and aquifer permeability.

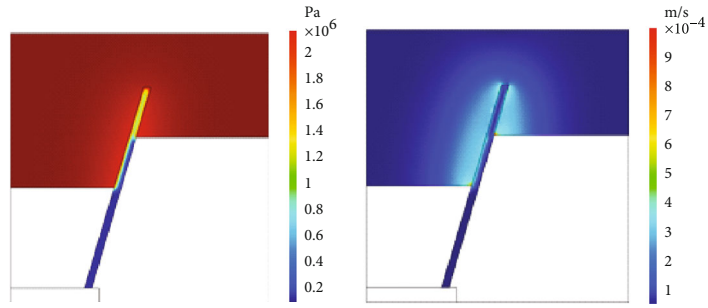

(a) Pressure cloud chart of 10 s (b) Velocity cloud chart of 10 s

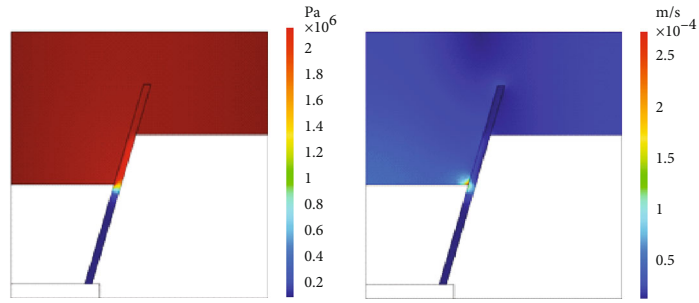

(c) Pressure cloud chart of 10^2 s (d) Velocity cloud chart of 10^2 s

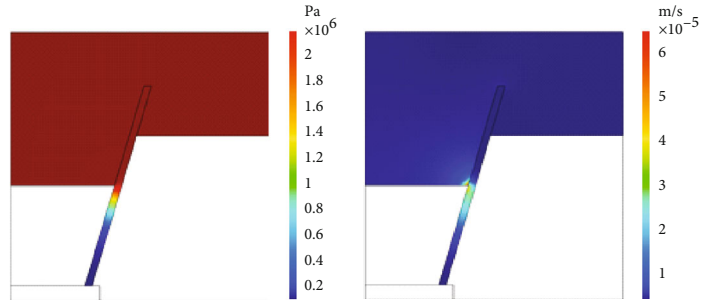

(e) Pressure cloud chart of 10^3 s (f) Velocity cloud chart of 10^3 s

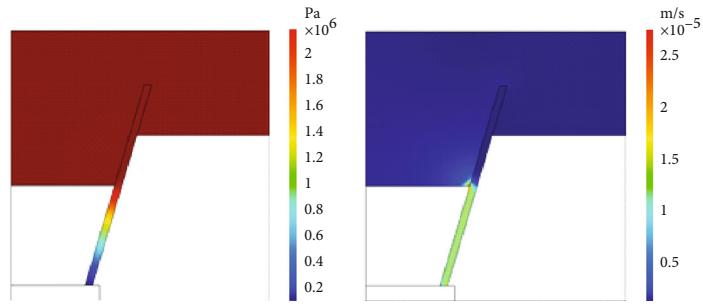

(g) Pressure cloud chart of 10^4 s (h) Velocity cloud chart of 10^4 s

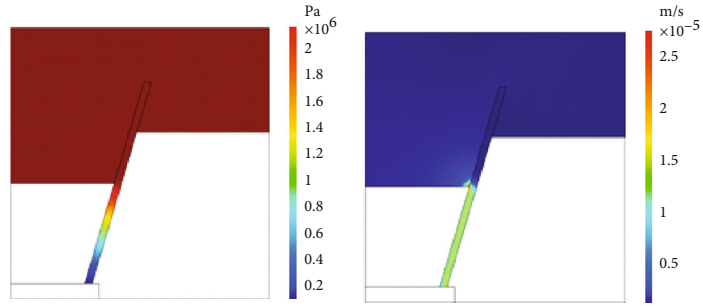

(i) Pressure cloud chart of 10^5 s (j) Velocity cloud chart of 10^5 s

Figure 20: Pressure and velocity cloud chart of fault under different transient conditions.

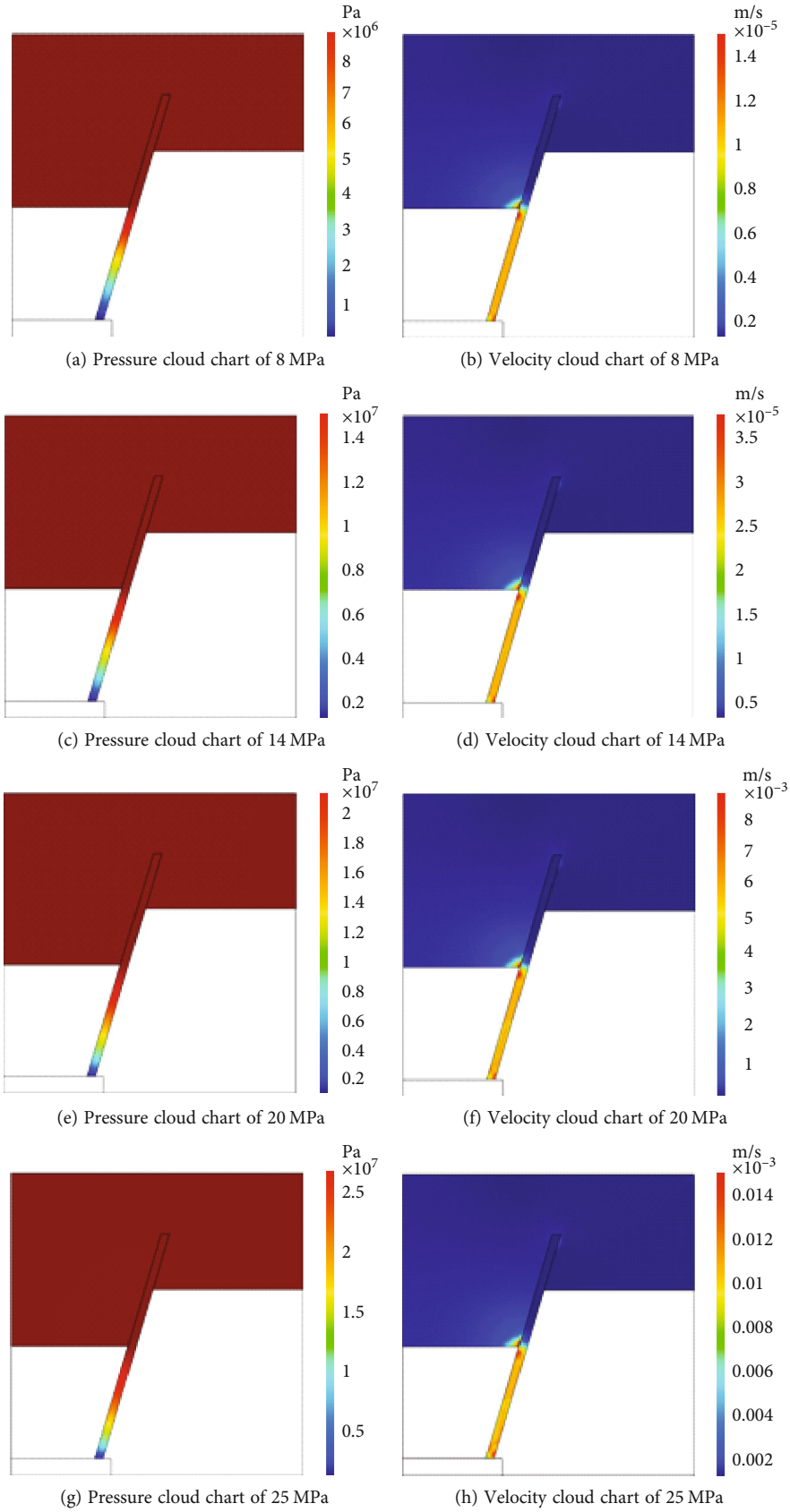

(a) Pressure cloud chart of 8 MPa

(b) Velocity cloud chart of 8 MPa

(c) Pressure cloud chart of 14 MPa

(d) Velocity cloud chart of 14 MPa

(e) Pressure cloud chart of 20 MPa

(f) Velocity cloud chart of 20 MPa

(g) Pressure cloud chart of 25 MPa

(h) Velocity cloud chart of 25 MPa

Figure 21: Pressure and velocity cloud chart of fault under different aquifer pressures.

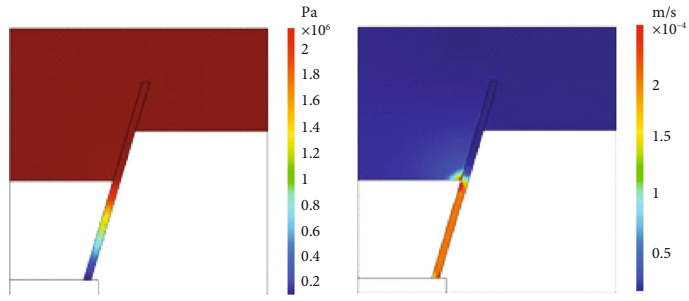

(a) Pressure cloud chart of $K = 0.1$

(b) Velocity cloud chart of $K = 0.1$

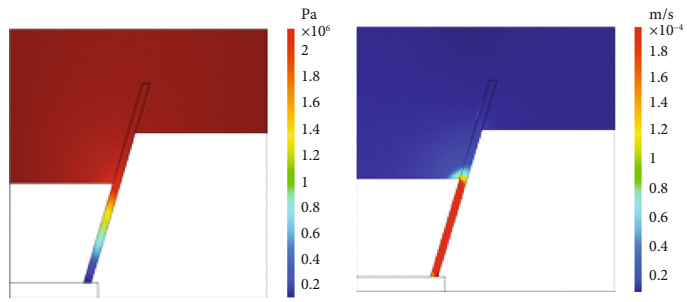

(c) Pressure cloud chart of $K = 1$

(d) Velocity cloud chart of $K = 1$

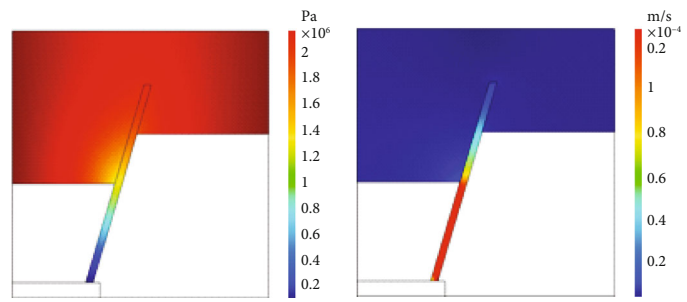

(e) Pressure cloud chart of $K = 10$

(f) Velocity cloud chart of $K = 10$

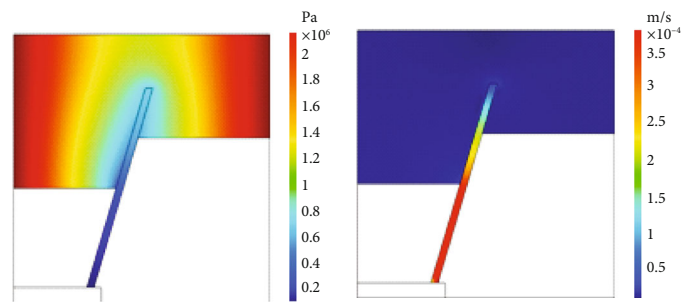

(g) Pressure cloud chart of $K = 100$

(h) Velocity cloud chart of $K = 100$

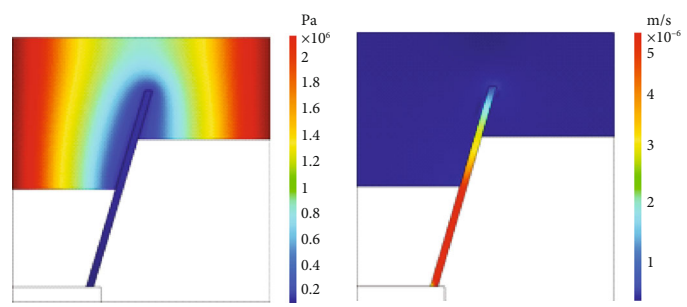

(i) Pressure cloud chart of $K = 1000$

(j) Velocity cloud chart of $K = 1000$

Figure 22: Pressure and velocity cloud chart of fault in different proportion of fracture zone permeability and aquifer permeability.

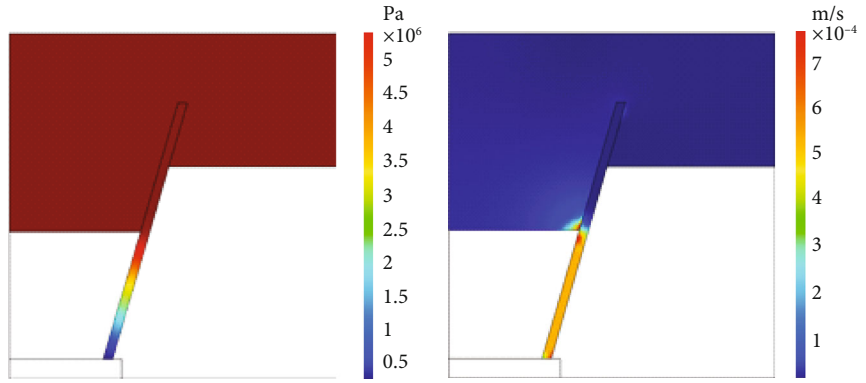

(a) Pressure cloud chart with 6×10^{-8} Pa^{-1} (b) Velocity cloud chart with 6×10^{-8} Pa^{-1}

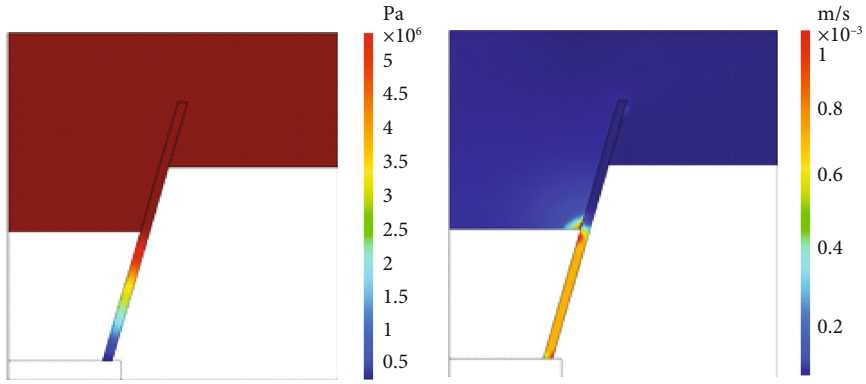

(c) Pressure cloud chart with 7×10^{-8} Pa^{-1} (d) Velocity cloud chart with 7×10^{-8} Pa^{-1}

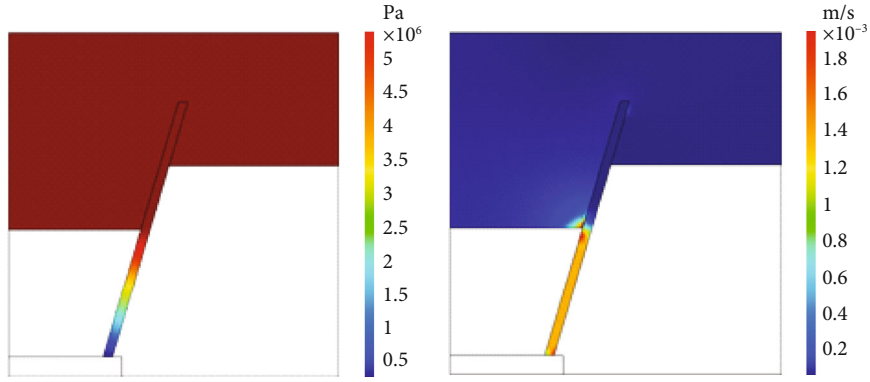

(e) Pressure cloud chart with 8×10^{-8} Pa^{-1} (f) Velocity cloud chart with 8×10^{-8} Pa^{-1}

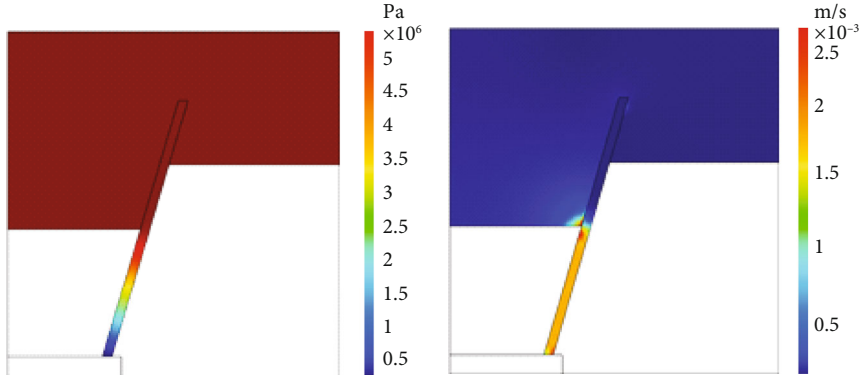

(g) Pressure cloud chart with 9×10^{-8} Pa^{-1} (h) Velocity cloud chart with 9×10^{-8} Pa^{-1}

Figure 23: Pressure and velocity cloud chart under different stress sensitivity coefficients.

apparent, and the range of values also expands. Additionally, it can be observed that proportional increases in the permeability within the fault zone's channel do not significantly impact the span of the color block on the chart. This means if the difference in permeability between the fault zone and the aquifer is large, any subsequent increase in permeability poses no serious risk of water inrush disasters. The velocity cloud chart also shows that as the permeability ratio rises, water velocity in the fault zone becomes more blocky. However, there is a threshold value beyond which velocity changes are negligible.

According to Figure 14, when the permeability ratio is small, the pressure velocity has no obvious change. When the permeability ratio increases to a certain extent, the water inflow speed at the junction of the fault zone and the roadway is no longer abrupt and is relatively gentle. In the aquifer, the flow velocity is generally small, but the closer to the fault zone passage, the faster the flow velocity will increase. It can be seen that, as the transition area of aquifer seepage and free flow of roadway, the channel of a fault fracture zone in the excavation section has an extremely obvious effect on the pressure and velocity of groundwater seepage. Combine the model with the actual excavation.

From the perspective of engineering practice, it is believed that the emergence of a water inrush disaster is the phenomenon that a lot of groundwater flows into the tunnel suddenly through the passage of a fault fracture zone by applying a constant pressure difference under the condition that the upper force passes through the aquifer and the aquifer has sufficient water. After the water flows through the edge of the channel of the fault zone, the groundwater runoff pressure with relatively low flow through a single fracture tends to concentrate, which is easy to increase the pressure, that is, the speed shown in the line graph increases. When the maximum value occurs, the increase of the fracture in the boundary aquifers, that is, the continuous increase of the permeability, will easily lead to water inrush accidents.

4.2.3. Fluid-Structure Coupling Analysis of Stress Sensitivity Coefficient of Pores in Different Fault Zones. The stress sensitivity coefficients of the pores in the fault zone were changed, which are, respectively, $5\times10^{-8}\,\mathrm{Pa}^{-1}$, $6\times10^{-8}\,\mathrm{Pa}^{-1}$, $7\times10^{-8}\,\mathrm{Pa}^{-1}$, $8\times10^{-8}\,\mathrm{Pa}^{-1}$, and $9\times10^{-8}\,\mathrm{Pa}^{-1}$.

According to Figures 15, 23 in Appendix, and 16, different stress sensitivity coefficients have little influence on the pressure of the roadway in the fault zone. The flow velocity is extremely small, and it is difficult to have water inrush accidents. At the joint of the fault zone and the roadway, we observe an abrupt increase in velocity. This phenomenon is caused by the contraction of the water section as it passes through the narrow opening between the fault zone and the roadway, resulting in a pressure boost. This pressure boost can have significant implications for the stability of the engineering structure, and further investigation is needed to fully understand its effects. Overall, our findings underscore the need for continued research into the dynamics of aquifer-fault zone systems, particularly in the context of engineering projects. By gaining a deeper understanding of these systems, we can develop more effective strategies for managing and mitigating the risks associated with geological hazards.

5. Conclusion

5.1. Analysis of Working Conditions. The initial pressure of an aquifer plays a critical role in the occurrence and evolution of water inrush incidents, particularly in underground mining and construction activities. When the initial pressure increases, the peak values of fluid pressure and velocity tend to increase, increasing the potential for water inrush accidents to occur. Proper monitoring and management of aquifer pressure are essential to minimize these risks and ensure safe and effective operations.

The roadway is connected to the aquifer through a fault zone, and the dip angle, permeability, and flow pattern in the fault zone play a key role in the changes in water inrush pressure and water inrush velocity. By comparing and analyzing the water pressure and flow velocity, it is found that the stress in the fault increases and the permeability decreases relatively in the fault. At the junction of the fault zone and the coal seam, the stress release area suddenly increases which leads to an increase in pore water pressure and seepage velocity. When the coal seam is mined near the fault, the stress is released. The sudden increase in permeability is the main reason for inducing fault-activated water inrush. The difference in permeability between rock and an aquifer determines whether water can flow. Different rock fracture zones and types of aquifers will affect the occurrence of water inrush. Comparing Darcy's law of seepage and fluid-structure coupling, it can be found that the solid effect of rock has a certain influence on the occurrence of water inrush disasters in the actual environment. At the junction of the fault and roadway, there is a sudden change of pressure and velocity under fluid-structure coupling. This shows the complexity and diversity of the actual project.

5.2. Prevention of Water Inrush. Water inrush caused by fault water flow caused by mining is the result of cumulative evolution over a period of time, and it does not happen suddenly without warning. Under the condition that there is an aquifer within the mining range of the mine, the groundwater pressure shall be monitored and predicted in time, and various influences such as the mining depth of the mine shall be fully considered according to the actual engineering problems. Measures such as properly retaining coal pillars and filling the goaf shall be taken to reduce the damage of coal mining to the upper rock mass, ensure that the groundwater is not affected, and ensure the safe production of coal under the mine. During the drainage and depressurization operation of the aquifer, the water inflow and water pressure of the borehole must be observed before the water inflow and water pressure are stabilized. After the water inflow and water pressure are basically stable, the construction shall be carried out according to the conventional observation needs.

Appendix

In this section, we present cloud maps of pressure and velocity under different conditions, as shown in Figures 17–23.

Data Availability

The data used to support the findings of this study are included within the article.

Conflicts of Interest

The authors declare that they have no conflicts of interest.

Acknowledgments

The authors are grateful to the financial support from the National Natural Science Foundation of China (12002270, 52274096, and 42007264), the Key Research and Development Program of Shaanxi Province, China (2022ZDLSF07-06, 2023-YBSF-369), the Natural Science Basic Research Program of Shaanxi (2022JC-LHJJ-08), the China Postdoctoral Science Foundation (2020M683686XB, 2020 M673451, 2021 T140553, and 2021 M692600), and the Youth Talent Promotion Project of the Xi'an Association for Science and Technology (095920211334).

References

[1] W. Tu, L. Li, C. Shang, S. Liu, and Y. Zhu, "Comprehensive risk assessment and engineering application of mine water inrush based on normal cloud model and local variable weight," *Energy Sources, Part A: Recovery, Utilization, and Environmental Effects*, pp. 1–16, 2019.

[2] Z. Song, Z. Zhang, P. G. Ranjith, W. Zhao, and C. Liu, "Experimental study on the influence of hydrostatic stress on the lode angle effect of porous rock," *International Journal of Mining Science and Technology*, vol. 32, no. 4, pp. 727–735, 2022.

[3] Y. Xue, S. Liu, J. Chai et al., "Effect of water-cooling shock on fracture initiation and morphology of high- temperature granite: application of hydraulic fracturing to enhanced geothermal systems," *Applied Energy*, vol. 337, article 120858, 2023.

[4] S. Zhang, W. Guo, Y. Li, W. Sun, and D. Yin, "Experimental simulation of fault water inrush channel evolution in a coal mine floor," *Mine Water and the Environment*, vol. 36, no. 3, pp. 443–451, 2017.

[5] Z. Ma, C. Zhang, R. P. Gamage, and G. Zhang, "Uncovering the creep deformation mechanism of rock-forming minerals using nanoindentation," *International Journal of Mining Science and Technology*, vol. 32, no. 2, pp. 283–294, 2022.

[6] Z. Ma, R. P. Gamage, and C. Zhang, "Mechanical properties of α-quartz using nanoindentation tests and molecular dynamics simulations," *International Journal of Rock Mechanics and Mining Sciences*, vol. 147, article 104878, 2021.

[7] P. Cheng, C. P. Zhang, Z. Y. Ma et al., "Experimental study of micromechanical properties alterations of shale matrix treated by ScCO2-water saturation using nanoindentation tests," *Energy*, vol. 242, article 122965, 2022.

[8] L. Li, W. Tu, S. Shi, J. Chen, and Y. Zhang, "Mechanism of water inrush in tunnel construction in karst area," *Geomatics, Natural Hazards and Risk*, vol. 7, supplement1, pp. 35–46, 2016.

[9] S. Wang, L. Li, S. Cheng et al., "Study on an improved real-time monitoring and fusion prewarning method for water inrush in tunnels," *Tunnelling and Underground Space Technology*, vol. 112, article 103884, 2021.

[10] Y. Xue, J. Liu, X. Liang et al., "Influence mechanism of brine-gas two-phase flow on sealing property of anisotropic caprock for hydrogen and carbon energy underground storage," *International Journal of Hydrogen Energy*, vol. 48, no. 30, pp. 11287–11302, 2023.

[11] Z. Burtan, A. Zorychta, J. Cieślik, and D. Chlebowski, "Influence of mining operating conditions on fault behavior," *Archives of Mining Sciences*, vol. 59, no. 3, pp. 691–704, 2014.

[12] J. Zhao and H. Konietzky, "An overview on flooding induced uplift for abandoned coal mines," *International Journal of Rock Mechanics and Mining Sciences*, vol. 148, article 104955, 2021.

[13] L. Li, M. Qian, and S. G. Li, "Mechanism of water-inrush through fault," *Mei Tan Hsueh Pao (Journal of China Coal Society)*, vol. 21, 1996.

[14] K. N. Dwarakanath and R. D. Blanton, "Universal fault simulation using fault tuples," in *Proceedings of the 37th Annual Design Automation Conference (pp. 786-789)*, Los Angeles California USA, 2000.

[15] P. Wang, L. Jiang, X. Li, G. Qin, and E. Wang, "Physical simulation of mining effect caused by a fault tectonic," *Arabian Journal of Geosciences*, vol. 11, no. 23, pp. 1–11, 2018.

[16] G. Chen, Y. Sun, Z. Xu, and X. Li, "Hydrogeological feasibility of mine water deep geological storage in Baotashan coarse sandstone: a case study in Ordos Basin," *Deep Underground Science and Engineering*, vol. 1, no. 2, pp. 148–164, 2022.

[17] H. L. Kong, X. X. Miao, L. Z. Wang, Y. Zhang, and Z. Q. Chen, "Analysis of the harmfulness of water-inrush from coal seam floor based on seepage instability theory," *Journal of China University of Mining and Technology*, vol. 17, no. 4, pp. 453–458, 2007.

[18] W. Liu, Q. Li, and J. Zhao, "Application on floor water inrush evaluation based on AHP variation coefficient method with GIS," *Geotechnical and Geological Engineering*, vol. 36, no. 5, pp. 2799–2808, 2018.

[19] L. Shi and R. N. Singh, "Study of mine water inrush from floor strata through faults," *Mine Water and the Environment*, vol. 20, no. 3, pp. 140–147, 2001.

[20] H. Yuan, C. Chen, Z. He, and Y. Wang, "Numerical simulation of fluid-solid coupling in surrounding rock for river stope mining," *Shock and Vibration*, vol. 2020, Article ID 9786182, 11 pages, 2020.

[21] J. Liu, Y. Xue, Y. Fu, K. Yao, and J. Liu, "Numerical investigation on microwave-thermal recovery of shale gas based on a fully coupled electromagnetic, heat transfer, and multiphase flow model," *Energy*, vol. 263, article 126090, 2023.

[22] H. Yin, S. Sang, D. Xie et al., "A numerical simulation technique to study fault activation characteristics during mining between fault bundles," *Environmental Earth Sciences*, vol. 78, no. 5, pp. 1–11, 2019.

[23] Z. H. Li, C. Z. Zhai, and L. F. Li, "Experimental study on water inrush mechanism due to floor faults activation in mining above confined aquifer," *Journal of Central South University (Science and Technology)*, vol. 46, no. 5, pp. 1806–1811, 2015.

[24] S. Ogata, H. Yasuhara, N. Kinoshita, and K. Kishida, "Coupled thermal–hydraulic–mechanical–chemical modeling for permeability evolution of rocks through fracture generation and subsequent sealing," *Computational Geosciences*, vol. 24, no. 5, pp. 1845–1864, 2020.

[25] Y. Yong, Y. Jian-hua, L. Jing, and Z. He-rui, "Online discrimination model for mine water inrush source based CNN and

fluorescence spectrum," *Spectroscopy and Spectral Analysis*, vol. 39, no. 8, pp. 2425–2430, 2019.

[26] Z. Zhao, J. Gu, and H. Zhang, "Study on the impact of the Argillation of fault filling on fault water inrush by a numerical model with heterogeneous media," *Geotechnical and Geological Engineering*, vol. 41, pp. 371–381, 2023.

[27] K. Wang, L. Wang, and B. Ren, "Failure mechanism analysis and support technology for roadway tunnel in fault fracture zone: a case study," *Energies*, vol. 14, no. 13, p. 3767, 2021.

[28] D. Ma, H. Duan, J. Zhang, and H. Bai, "A state-of-the-art review on rock seepage mechanism of water inrush disaster in coal mines," *International Journal of Coal Science & Technology*, vol. 9, no. 1, p. 50, 2022.

[29] V. Maronnier, M. Picasso, and J. Rappaz, "Numerical simulation of free surface flows," *Journal of Computational Physics*, vol. 155, no. 2, pp. 439–455, 1999.

[30] Y. Xue, P. G. Ranjith, F. Gao, Z. Zhang, and S. Wang, "Experimental investigations on effects of gas pressure on mechanical behaviors and failure characteristic of coals," *Journal of Rock Mechanics and Geotechnical Engineering*, vol. 15, no. 2, pp. 412–428, 2023.

[31] M. Qiu, J. Han, Y. Zhou, and L. Shi, "Prediction reliability of water inrush through the coal mine floor," *Mine Water and the Environment*, vol. 36, no. 2, pp. 217–225, 2017.

[32] J. Zhao, L. Bo, C. Juntao, and J. Ning, "Mechanism of seepage-stress fault water inrush and grouting seal," *Arabian Journal of Geosciences*, vol. 13, no. 11, pp. 1–12, 2020.

[33] M. Sedghi-Asl, H. Rahimi, and R. Salehi, "Non-Darcy flow of water through a packed column test," *Transport in Porous Media*, vol. 101, no. 2, pp. 215–227, 2014.

[34] H. Kang, W. Li, F. Gao, and J. Yang, "Grouting theories and technologies for the reinforcement of fractured rocks surrounding deep roadways," *Deep Underground Science and Engineering*, vol. 2, no. 1, pp. 2–19, 2023.

[35] L. Shi, M. Qiu, C. Teng, Y. Wang, T. Liu, and X. Qu, "Risk assessment of water inrush to coal seams from underlying aquifer by an innovative combination of the TFN-AHP and TOPSIS techniques," *Arabian Journal of Geosciences*, vol. 13, no. 14, pp. 1–18, 2020.